Subsonic Steady and Oscillatory Aerodynamics for Multiple Interfering Wings and Bodies

J. P. GIESING,* T. P. KÁLMÁN,† AND W. P. RODDEN‡
Douglas Aircraft Company, McDonnell Douglas Corporation, Long Beach, Calif.

A technique for predicting steady and oscillatory aerodynamic loadings on general configurations is presented for use in flutter, gust, and static aeroelastic analyses and estimation of static and dynamic stability derivatives. The procedures are based on the Doublet-Lattice Method and the method of images. Chordwise and spanwise load distributions on lifting surfaces and longitudinal load distributions on bodies are determined for configurations that consist of an assemblage of bodies (with variable circular or elliptic cross sections) and lifting surfaces (with arbitrary planform and dihedral, with or without control surfaces). Extensive comparisons are made with steady and oscillatory experimental lifting pressure data.

Nomenclature

a, b = length of semimajor and semiminor axes, respectively, of body cross section; applies to constant cross-sectional tube idealization
$a_0(\xi)b_0(\xi)$ = same as a, b except represents a distribution of local values of semimajor and minor lengths; used for slender body idealization
C_p = pressure coefficient $(p - p_\infty)/q$
c = local chord length
$\bar{c}$ = reference chord length
D = influence matrix relating normalwash to lifting pressure
d = lateral or vertical distance from body axis, used to locate doublet or vortex pairs
E_r = influence matrix relating normalwash to body axis singularities for the residual flow
E_{sb} = influence matrix relating normalwash to body axis singularities for slender body flow
e = semiwidth of lifting surface element
F = total force on a body
$H_\nu^{(2)}(\bar{k})$ = Hankel function of second kind, order ν, of argument $\bar{k}$
$\mathbf{i}_r$ = unit vector in direction of r_a
$\mathbf{i}_{\vec{r}}$ = unit vector in direction of r
$\mathbf{i}_\theta$ = unit vector normal to $\mathbf{i}_r$
$\mathbf{i}_{\vec{\theta}}$ = unit vector normal to $\mathbf{i}_{\vec{r}}$
K = lifting surface kernel function giving the normalwash at a point due to a point *pressure* doublet of unit strength
k_r = reduced frequency, $\omega\bar{c}/2U$
$\bar{k}$ = $\omega r M/U$
L = function giving the normalwash at a point due to a point doublet of unit strength
M = Mach Number
$\mathbf{N}$ = direction of point pressure doublet
R = distance from a point singularity to a general field point
R_a = distance from a point pressure doublet to a point on the axis of a body
r = two-dimensional distance from a point singularity to a general field point
r_a = two-dimensional distance from a point pressure doublet to the axis of a body
s = lateral distance along a lifting surface
U = freestream speed
w = normalwash; velocity normal to a lifting surface or velocity in the y- or z-direction to a body
x,y,z = coordinates of a general field point
α = angle-of-attack
β = $(1 - M^2)^{1/2}$
ΔC_p = lifting pressure coefficient $(p_{\text{lower}}\text{-}p_{\text{upper}})/q$
$\Delta\xi$ = body element length
δA = area of lifting surface element
δw = residual flow normal to a body surface
$\overline{\delta w}$ = average of δw
θ = body cross-sectional angular coordinate. Equation for body cross section $y = a_0 \cos\theta$, $z = b_0 \sin\theta$
λ = $\omega M/\beta U$
μ = doublet strength per unit length of body axis
$\tilde{\mu}$ = $2\mu \exp[i\omega(\xi - \xi_c)/U]$
μ_2 = quadrupole strength
ξ,η,ζ = coordinate of a point pressure doublet
ω = frequency of oscillation

Subscripts and Superscripts

a = body axis
I = image point
r = residual flow
sb = slender body flow

Introduction

THERE are many types of analyses that use steady and oscillatory aerodynamic loads. Among these are flutter, gust, frequency response, and static aeroelastic analyses. In addition, static and dynamic stability derivatives and transient response (through the use of the inverse Fourier transformation) can be determined by such loads. Therefore, it is important that aerodynamic loads be predicted as accurately and efficiently as possible, and it is toward these ends that this paper is directed.

The classic approach to the unsteady compressible flow problem has been through the use of a lifting surface theory. There are basically two classes of lifting surface theories: the traditional kernel function technique, and the finite element method. The vortex and doublet-lattice finite element methods are achieving wide acceptance because of their simplicity, accuracy, and versatility, and it is upon these methods that the present method is based.

Many authors have contributed to the development of both classes of lifting surface theories, and several of the more recent contributions include the methods for steady flow of Hedman,[1] Giesing,[2] Woodward,[3] Spangler and Mendenhall,[4] Borland[5] and Chou[6] and the methods for unsteady flow of Laschka,[7] Zwaan,[8] Albano and Rodden,[9] Stark,[10] Kálmán et al.,[11] Albano et al.,[12] and Rodden et al.[13]

Presented as Paper 72-26 at the AIAA 10th Aerospace Sciences Meeting, San Diego, Calif., January 17–19, 1972; submitted May 24, 1972. This paper summarizes work performed for the Aerospace Dynamics Branch, Vehicle Dynamics Division, Air Force Flight Dynamics Laboratory, Wright-Patterson Air Force Base, Ohio, under Contract F33615-70-C-1167, Project 1370, and Task 137003.

Index categories: Airplane and Component Aerodynamics; Aeroelasticity and Hydroelasticity; Nonsteady Aerodynamics.

* Senior Group Engineer, Structural Mechanics Section. Associate Fellow AIAA.

† Engineer Scientist Specialist, Structural Mechanics Section. Member AIAA.

‡ Consulting Engineer. Associate Fellow AIAA.

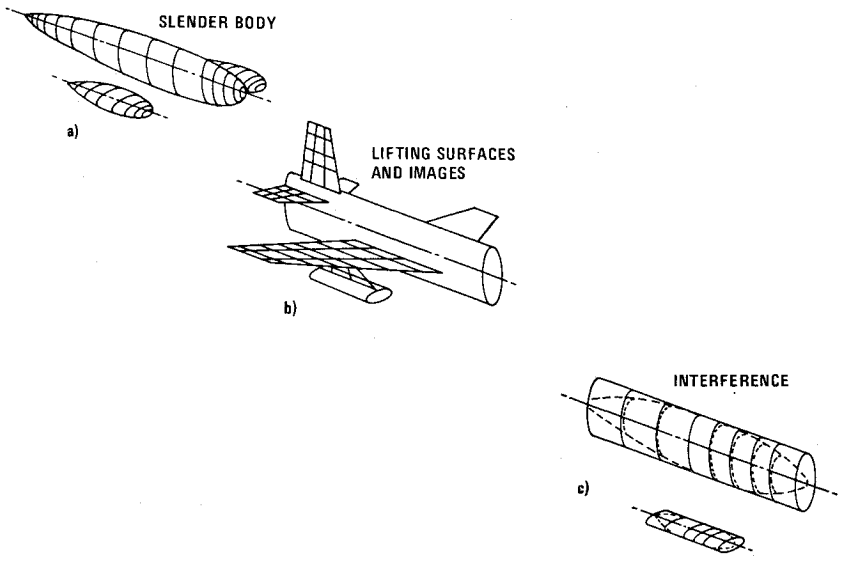

Fig. 1 Configuration idealization.

In the steady flow case the effects of bodies have been included by Giesing,[2] Spangler and Mendenhall,[4] Borland,[5] and Chou[6] through the use of images, and by Woodward[3] through the use of lifting surface elements on the body surface. For most of these methods an axial singularity distribution is added to account for body volume, angle-of-attack, and camber (slender body) effects.

Basically two idealizations are introduced for the body: 1) an equivalent axisymmetric body is used to represent the slender body effects, and 2) a constant-section tube is used for body lifting-surface interference effects. A constant-section tube must be used because of the nature of the lifting surface singularity, and because the body surface boundary condition is linearized.

The unsteady lifting surface theories of Laschka,[7] Zwaan,[8] Albano and Rodden,[9] Stark,[10] and Albano et al.[12] do not account for the effects of bodies. Bodies are considered in a limited way in Ref. 11 and more generally in Ref. 13. In the method of Ref. 13, unsteady lifting surface elements are placed on an idealized body surface in the same way that they are placed in the steady Woodward method. This method requires many elements on the body surface to produce an accurate result. If more than one body is involved, the total number of elements, which include those on the lifting surfaces, may become excessively large for present-generation computers.

The present method is introduced to provide an accurate and efficient unsteady lifting surface theory for configurations involving multiple lifting surfaces and multiple bodies. The method uses an unsteady image system to eliminate the need for lifting surface elements on the body surface. Because of this, many bodies may be handled without an excessive amount of computational effort. Unlike many image methods, body cross sections are not restricted to circular shapes, but may be elliptical. Also, a new method of obtaining the longitudinal distribution of load on the bodies has been devised.

Other methods exist for handling general configurations; however, they are all restricted in various ways. For instance, there are the methods of Rubbert and Saaris,[14] Labrujere et al.,[15] and Hess.[16] The exact configuration is used without any idealization (no linearization of the boundary conditions). These methods determine detailed surface pressures and not just load distributions and are strictly valid only for incompressible flow, since the Laplace equation is obtained directly without linearization. In practice, the Glauert transformation is applied to obtain Mach number effects; however, this transformation is valid only for configurations that produce small perturbations to the flow.

The basic restriction of these methods is that they apply only in steady flow. An extension to unsteady (incompressible) flow was made by Giesing[17]; however, this method is restricted to two dimensions.

There are several other steady-flow methods that are hybrid in nature. Monical[18] and Tulinius[19] have developed steady, incompressible, flow methods that are based on the assumption that only the wing thickness is small while the camber deflections may be large.

Outline of the Theory

Doublet-Lattice Method

One of the basic building blocks of the present approach is the Doublet-Lattice Method (DLM) developed for interfering lifting surfaces oscillating in subsonic flow. The DLM is a finite-element lifting-surface theory that reduces to the Vortex-Lattice Method in steady flow. The technique is applicable to combinations of wings with arbitrary planform and dihedral including control surfaces, and has been proven by extensive correlations with other theories and experimental data.[9,11,13,20-23]

The theory is well documented elsewhere[9,13,20,23] and need not be presented here. It is sufficient to note that the flow singularities used to model the lifting surface are steady horseshoe vortices and oscillatory line doublets superimposed on the bound vortex. The idealization of each lifting surface consists of its division into small trapezoidal elements (boxes) arranged in strips parallel to the freestream [see Fig. 1(b)] such that surface edges, fold lines, and control surface edges lie on box boundaries. To represent the steady flow effects, a horseshoe vortex is located on each box such that its bound leg lies along the quarter-chord line of the box, and to represent the oscillatory increment, a uniform line of acceleration potential doublets (with the steady doublet strength subtracted) is added to the bound vortex. The total effect of the vortex and incremental oscillatory doublet is given by an influence function D_{ij} that relates the complex amplitude of pressure coefficient of each box (which acts at the one-quarter-chord centerline) to the complex amplitude of the normalwash at each control point (which is located at the three-quarter-chord centerline). The influence of all pressure coefficients on all control points when summed leads to a system of simultaneous complex equations for the unknown pressure coefficients, ΔC_p, in terms of the distribution of normalwash, w, and their solution for a prescribed normalwash yields the desired pressure coefficients. In matrix form this can be expressed as

$$\{w\} = [D]\{\Delta C_p\} \tag{1}$$

Modified Slender Body Theory

The basic concepts of slender body theory§ are used to determine the axial distributions of both force and flowfield near the body. An extension of this approach is required because far field flow effects are required to account properly for the effects of the bodies on the lifting surfaces and other bodies.

The incremental normalwash, Δw, at points lying on the lifting surface due to a body, can be obtained from a distribution of singularities along the body axis. The singularities are in the form of a multipole expansion. If the body cross section has two planes of symmetry and the onset flow w is uniform, then the multipole expansion consists of doublets, quadrupoles, etc.

$$\Delta w(x,y,z) = \frac{1}{4\pi}\int_{\text{Body}} \left\{\mu(\xi)L + \mu_2(\xi)\frac{\partial^2 L}{\partial N^2} + \cdots\right\} d\xi \quad (2)$$

where $L = L(x-\xi, y-\eta_a, z-\zeta_a, \omega, M)$ is the normalwash at x,y,z due to a doublet of unit strength (not a pressure doublet) located at ξ,η_a,ζ_a and oriented in the direction N. The subscript a indicates the body axis. The kernel L represents the complete solution to the unsteady compressible three-dimensional differential equation and is related to K as follows

$$K(x-\xi_1,\ldots) = \int_{\xi_1}^{\infty} \exp[-i\omega(\xi-\xi_1)/U]L(x-\xi,\ldots)d\xi \quad (3)$$

The kernel K represents the normalwash due to a pressure doublet of unit strength located at ξ_1,η_a,ζ_a. Equation (3) shows that a pressure doublet is actually a semi-infinite line doublet (origin at ξ_1) whose strength varies like $\exp[-i\omega(\xi-\xi_1)/U]$.

Slender body theory assumes that the flow near the body is quasi-steady and two-dimensional. Thus, the multipole strengths, $\mu(\xi)$, $\mu_2(\xi)$ etc., can be obtained using simple solutions of the two-dimensional Laplace equation. The additional source solution usually obtained for steady flow does not exist in unsteady flow since the body does not change in volume with time.

For an elliptic cross section whose semimajor and semiminor axes are $a_0(\xi)$ and $b_0(\xi)$, respectively,

$$\mu(\xi) = w(\xi)\pi a_0(\xi)[a_0(\xi) + b_0(\xi)] \quad (4a)$$

$$\mu_2(\xi) = w(\xi)(\pi/4)a_0(\xi)[a_0(\xi) + b_0(\xi)]^2[a_0(\xi) - b_0(\xi)] \quad (4b)$$

Here, $w(\xi)$ is the local upwash along the body axis. Rather than derive new formulas for each term in the multipole expansion, an attempt is made to use the existing lifting surface kernel K to simulate the multipoles, through the second (quadrupole) term. The effect of the quadrupole is obtained in either one of two ways: 1) for $b_0/a_0 > 1$, one doublet is placed above the axis a distance d, while another is placed below the axis the same distance, 2) for $b_0/a_0 < 1$, the doublet is integrated in the horizontal direction from $-d$ to $+d$ (see Fig. 2). In two dimensions, the latter is a pair of vortices: one at $-d$ of strength $\mu/2d$, and one at $+d$ of the opposite sign. The incremental normalwash is then

$$\Delta w = (1/4\pi)\int_{\text{Body}} \mu(\xi)\bar{L}d\xi \quad (5)$$

where

$$\bar{L} = \begin{cases} [L(\ldots, z-\zeta_a-d,\ldots) \\ \quad + L(\ldots, z-\zeta_a+d,\ldots)]1/2, & b_0/a_0 > 1 \\ (1/2d)\int_{-d}^{d} L d\eta \quad , & b_0/a_0 < 1 \end{cases} \quad (6)$$

§ The slender body forces are obtained using the slender body theory of Miles.[24]

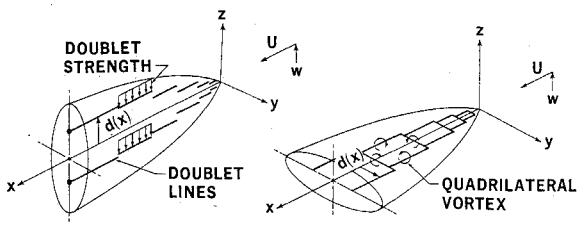

Fig. 2 Idealization of body axis singularities.

in which

$$d = \begin{cases} (b_0^2 - a_0^2)^{1/2}/2 \quad , & b_0/a_0 > 1 \\ [3(a_0^2 - b_0^2)]^{1/2}/2, & b_0/a_0 < 1 \end{cases} \quad (7)$$

and where $\mu(\xi)$ is given by Eq. (4a). Equation (5) then simulates the multipole expansion through the second term.

A finite element approach is again taken with Eq. (5) where the body is divided into elements (see Fig. 2). The leading and trailing edges of element j are ξ_{1j} and ξ_{2j}, respectively. Then

$$\Delta w = (1/4\pi)\sum_{j=1} \int_{\xi_{1j}}^{\xi_{2j}} \mu\bar{L}d\xi \quad (8)$$

If a new variable $\tilde{\mu}$ is introduced such that

$$\mu = (\tilde{\mu}/2)\exp[-i\omega(\xi-\xi_c)/U] \quad (9)$$

where $\xi_c = (\xi_1+\xi_2)/2$ is the location of the element center, and if $\tilde{\mu}$ is held constant over each element then Eq. (8) becomes

$$\Delta w = \sum_{j=1} \tilde{\mu}_j E_{ij} \quad (10)$$

or in matrix form

$$\{\Delta w\} = [E]\{\tilde{\mu}\} \quad (11)$$

The influence coefficient E_{ij} is obtained when $\tilde{\mu}$ is introduced into Eq. (8). Defining $\Delta\xi = \xi_2 - \xi_1$, such that $\xi_c = \xi_1 + \Delta\xi/2 = \xi_2 - \Delta\xi/2$, permits the expression for E_{ij} to be written as

$$E_{ij} = (1/8\pi)\left\{\exp(i\omega\Delta\xi_j/2U)\int_{\xi_{1j}}^{\infty} \exp[-i\omega(\xi-\xi_{1j})/U]\bar{L}_{ij}d\xi - \exp(-i\omega\Delta\xi_j/2U)\int_{\xi_{2j}}^{\infty} \exp[-i\omega(\xi-\xi_{2j})/U]\bar{L}_{ij}d\xi\right\} \quad (12)$$

Referring back to the relation between L and K, Eq. (3), it becomes apparent that E_{ij} may be written in terms of K or an integral of K.

$$E_{ij} = (1/8\pi)[\exp(i\omega\Delta\xi_j/2U)\bar{K}(x-\xi_1,\ldots) - \exp(-i\omega\Delta\xi_j/2U)\bar{K}(x-\xi_2,\ldots)] \quad (13)$$

where

$$\bar{K} = \begin{cases} [K(\ldots, z-\zeta_a-d,\ldots) \\ \quad + K(\ldots, z-\zeta_a+d,\ldots)]/2, & b_0/a_0 > 1 \\ (1/2d)\int_{-d}^{d} K d\eta \quad , & b_0/a_0 < 1 \end{cases}$$

The integral given for $\bar{K}$ above is exactly $D_{ij}/\Delta\xi$ with the lifting surface element half width e_j replaced with d_j. Thus, the equation for the normalwash flow field about a body of elliptic cross section has been expressed in terms of known quantities, i.e., K, D, and a_0, b_0.

Equation (13) represents the sum of two pressure-type singularities: one located at ξ_1 and one at ξ_2. Each of these possesses a wake; however, the wake from the one located at

ξ_1 is canceled by the one located at ξ_2, aft of the point ξ_2. The result is a finite length singularity possessing no wake aft of ξ_2 (see Fig. 2). For the case $b_0/a_0 > 1$, the singularity is composed of two finite length line doublets. For the case $b_0/a_0 < 1$, the singularity is an unsteady trapezoidal vortex which is also shown in Fig. 2.

Interference

The first step in the determination of interference has been taken. Specifically, the incremental normalwash Δw due to isolated bodies has been found. The resulting normalwash is

$$\{w_T\} = \{w\} - \{\Delta w\} \tag{14}$$

and is known at all lifting surfaces and bodies. This may be viewed as a new normalwash distribution to be satisfied by the lifting surfaces and bodies and need not be considered further: simply replace w with w_T.

The approach to be taken in the solution of this new modified boundary value problem is to: 1) generate an approximate Green's function for lifting surfaces in the presence of several bodies, and 2) generate a residual flow used to render the Green's function exact. In simpler terms, an image system is generated within each body to divert the flow around that body when it is in the presence of the lifting surface. The image system is not completely effective in doing this, however, and a residual flow must be added. The residual potential is a simple axial singularity distribution very similar to the axial system discussed in the previous section.

The method of images is well known. Lennertz[25] and Koeing[26] were two of the first to use the method for steady flow. The basic idea of the method is to match each singularity external to the body with one internal to the body at the "image" point. The strength of the internal or image singularity is directly related to that of the external singularity strength so that no new unknown distributions are introduced. The image singularity exists to negate the flow through the body surface generated by the external singularity. The method of images has been used in various ways. Most investigations have neglected the residual flow; however, Rethorst[27] and Wu and Talmadge[28] have generated complicated expressions for the residual flowfields. Recent refinements and extensions have been made by Borland[5] and Chou.[6]

Since all the singularities discussed here (except the source) can be reduced to a pressure doublet or an integrated pressure doublet, only an expression for the image point (η_1,ζ_1) and image strength $(\tilde{\mu}_1)$ of a pressure doublet will be presented.

$$\left.\begin{aligned} \eta_1 &= (a^2/r_a{}^2)\eta \\ \zeta_1 &= (a^2/r_a{}^2)\zeta \\ \tilde{\mu}_1{}^{(y)} &= -(a^2/r_a{}^4)[\tilde{\mu}^{(y)}(\eta^2 - \zeta^2) + \tilde{\mu}^{(z)}2\zeta\eta] \\ \tilde{\mu}_1{}^{(z)} &= (a^2/r_a{}^4)[\tilde{\mu}^{(z)}(\eta^2 - \zeta^2) + \tilde{\mu}^{(y)}2\zeta\eta] \end{aligned}\right\} \tag{15}$$

where r_a is the radial two-dimensional distance from the cross-section axis to the doublet, whose strength is $\tilde{\mu}^{(y)}\mathbf{j} + \tilde{\mu}^{(z)}\mathbf{k}$, located at (η,ζ). Equation (15) is valid only for a circular cross section. An extension to elliptic cross sections was made by Borland[5] using conformal transformation methods. An alternate approach is taken here which is based on the local surface radius and center of curvature of the ellipse. The first step is to find the elliptic coordinates of the pressure doublet. Curves of constant elliptic coordinates are ellipses and hyperbolas. The next step is to find the intersection of the hyperbola with the actual elliptic surface. This is the point at which the radius and center of curvature are determined. The ellipse is then replaced by a circle that has a radius and center corresponding to the radius and center of curvature of the ellipse. Other doublets lie on other hyperbolas and thus require different circles for their images. This method is restricted to moderate cross-sectional aspect ratios (b/a) since in extreme cases the image may fall outside of the cross section. Accuracy is also lost if images from the right wing fall on top of images from the left wing within a fuselage. In this case the overlap is eliminated by requiring images of points lying in a particular quadrant, in a coordinate system centered in the body, to lie in the same quadrant within the body.

The image approach just outlined is unaltered for the oscillatory case. In all three-dimensional cases, steady or unsteady, the image does not satisfy the boundary condition on the body surface exactly and, thus, a residual flow is required. The image system exists to eliminate the singularities in normalwash at points on the body surface lying adjacent to lifting surfaces. Once the flow about the body is regularized, a slender body theory can be used to complete the body surface boundary condition. The residual flow caused by unsteadiness is of the same order as the residual flow caused by the three-dimensionality and cross-sectional aspect ratio (b/a); thus, it does not require special consideration.

In general, an image of an external singularity must be placed in each body. However, if the singularity lies at a moderate distance from a particular body, it need not have an image for that body; its effect can be accommodated by the residual flowfield.

The image approach requires that the body cross section be constant downstream of the external singularity. Because of this, a constant section tube must be used for the image system. Figure 1 shows that the lifting surfaces must be attached to these tubes. There are, then, two idealizations for the body: one for slender body effects (body of varying width or radius), and one for images (constant section tube). The residual flow will use both of these idealizations. The residual onset flow generated by the lifting surfaces and images is determined at the surface of the constant section tube. However, this residual onset flow is then applied at the actual body surface.

Since the slender body approach is used to determine the residual flow, the problem is again reduced to a quasi steady two-dimensional problem. The basic difference between the determination of the residual flow and the flow due to the slender body is that the onset flow, δw, is not uniform in the residual case, but varies around the circumference of the body. The doublet and quadrupole strengths are now functions of onset flow variation. The distance d used to generate the proper quadruple for the body in uniform flow, however, is already fixed. If it is assumed that the residual flow, δw, is small compared to the slender body flowfield¶ Δw then the residual flow need not be represented as accurately as that due to the slender body. Specifically, the multipole expansion is matched only through the first (doublet) term. The doublet strength μ is determined from Eq. (4a) once w is known. Since the onset flow, δw, is not uniform, an average onset velocity, $\overline{\delta w}$, must be determined. The average $\overline{\delta w}$ is then used in place of w in Eq. (4a). This average is obtained as follows

$$\overline{\delta w^{(y)}} = (1/\pi)\int_0^{2\pi} f\delta w \cos\theta d\theta \tag{16}$$

$$\overline{\delta w^{(z)}} = (1/\pi)\int_0^{2\pi} f\delta w \sin\theta d\theta \tag{17}$$

where $f = [\sin^2\theta + (b/a)^2\cos^2\theta]^{1/2}$. The term δw is the residual onset flow normal to the elliptic cross-sectional surface. The angular coordinate θ is related to the elliptic surface as follows: $y(\theta) = a\cos\theta$, $z(\theta) = b\sin\theta$. The average velocities to the body in the z- and y-directions, i.e., $\overline{\delta w^{(y)}}$ and $\overline{\delta w^{(z)}}$, due to the residual onset flow δw, are applied to the

¶ There is evidence that the residual flow is small and in many cases can be neglected altogether thus saving computational effort.

actual body surface through Eq. (4a) to give the proper doublet strength. This doublet strength is used through Eq. (11) to produce the effects of the residual flow at all points of interest in the flowfield (e.g., normal to the lifting surfaces, etc.).

Solution

The problem to solve may be cast into the following matrix form

$$\{w_T\} = [D \vdots E_r]\begin{Bmatrix}\Delta C_p \\ \cdots \\ \tilde{\mu}_r^{(z)} \\ \cdots \\ \tilde{\mu}_r^{(y)}\end{Bmatrix} \tag{18}$$

where the known values of w_T are given by

$$\{w_T\} = \{w\} - [E_{sb}]\begin{Bmatrix}\tilde{\mu}_{sb}^{(z)} \\ \cdots \\ \tilde{\mu}_{sb}^{(y)}\end{Bmatrix} \tag{19}$$

The subscripts sb and r have been introduced on E and $\tilde{\mu}$ to indicate the difference between slender body doublets and residual flow doublets. The terms $\tilde{\mu}_r^{(z)}$ and $\tilde{\mu}_r^{(y)}$ are the residual interference doublet strengths, and E_r represents their effects on the lifting surface and body boundary conditions. The terms $\tilde{\mu}_{sb}^{(z)}$ and $\tilde{\mu}_{sb}^{(y)}$ are the slender body doublet strengths, and E_{sb} represents their effects of the lifting surface and body boundary conditions. Because slender body theory is used to represent the effects of the bodies, a doublet at one axial location does not affect the boundary condition at another location on the same body. It does, however, affect other bodies. The matrix $[D]$ which represents the normalwash of lifting surface elements on themselves has been generalized in Eq. (18) to include the y- and z-wash at interference body elements due to lifting surface elements.

Equation (18) represents a set of simultaneous equations that may be so solved for the unknowns, ΔC_p, $\tilde{\mu}_r^{(z)}$ and $\tilde{\mu}_r^{(y)}$, in terms of the known boundary conditions, w_T. The lifting pressure distribution, ΔC_p, can be integrated to give the lifting surface contributions to the aerodynamic parameters of interest (span loading, a.c., c.p., generalized forces, etc.). The forces on the bodies, however are determined in a more complicated manner.

Body Forces

Each singularity contributes to the force distribution on each body. Every lifting surface box, every image, and every body axis doublet affects the force distributions. As outlined in the previous sections, every singularity can be obtained from the point pressure doublet whose normalwash flowfield is obtained from the standard lifting surface kernel K. An analytic expression exists for the pressure field due to a point pressure doublet and is:

$$C_p(x,y,z) = \frac{\Delta C_p(\xi,\eta,\zeta)\delta A}{4\pi}\exp[i\lambda M(x-\xi)]\frac{\partial}{\partial N}\left\{\frac{e^{-i\lambda R}}{R}\right\} \tag{20}$$

where $R^2 = (x-\xi)^2 + \beta^2 r^2$, $\lambda = \omega M/U\beta$ and $\mathbf{N}$ is the unit vector in the direction of the doublet. The term $\Delta C_p(\xi,\eta,\zeta)\delta A$ is the total pressure doublet strength of a lifting surface element of area δA and lifting pressure of ΔC_p located at ξ,η,ζ. An equivalent point pressure doublet is assumed to act along the element center at the $\frac{1}{4}$-chord point. Actually, $\Delta C_p \delta A$ is used to represent all pressure doublet strengths. As stated previously, the finite length body doublet is composed of two pressure doublets, one located at the leading edge of the element, whose strength is $\tilde{\mu}\exp[i\omega\Delta\xi/2U]$, and one located at the trailing edge whose strength is $-\tilde{\mu}\exp[-i\omega\Delta\xi/2U]$. Thus, there are two pressure doublets per body element.

Equation (20) must be integrated over the body surface to obtain the forces acting on the body due to the equivalent pressure doublet located at ξ,η,ζ. The effects of all pressure doublets must then be summed to obtain the total.

Equation (20) can be integrated analytically only for special cases. For instance, it may be integrated in the x-direction from $-\infty$ to $+\infty$. A circumferential integration then produces the total force and moment on a body of constant cross section (of arbitrary shape):

$$\mathbf{F}/q = \frac{\Delta C_p \delta A}{(2\pi)}\oint f(\bar{k})\frac{(\mathbf{i}_r \cdot \mathbf{N})}{r}\mathbf{n}ds \tag{21}$$

$$\mathbf{M}/q = \frac{\Delta C_p \delta A}{(2\pi)}\oint p(\bar{k})(\mathbf{i}_r \cdot \mathbf{N})\mathbf{n}ds \tag{22}$$

where $f(\bar{k}) = -i(\pi/2)\bar{k}H_1^{(2)}(\bar{k})$; $p(\bar{k}) = M(\pi/2)\bar{k}H_0^{(2)}(\bar{k})$; $\bar{k} = \omega Mr/U$; $\mathbf{r} = \mathbf{i}_r r = \mathbf{j}(y-n) + \mathbf{k}(z-\zeta)$; $\mathbf{n}$ = cross-sectional surface outward normal vector; $H_\nu^{(2)}(\bar{k})$ = Hankel function of second kind. Details of this integration are found in Ref. 22, Appendix D. The circuit integral is to be taken around the cross section. Presently, this integration is done numerically for elliptic cross sections; however, it can be done easily for any cross section. The circuit integrals in Eqs. (21) and (22) can be integrated analytically for the steady case $f(\bar{k}) \to 1$, $p(\bar{k}) \to 0$ and circular cross sections (see Ref. 22, Appendix F). The result is

$$\begin{aligned}\mathbf{F}/q &= \frac{\Delta C_p \delta A}{(2)}\mathbf{N}, \quad r_a < a_0 \\ \mathbf{F}/q &= \frac{\Delta C_p \delta A}{(2)}\{\mathbf{i}_\theta N_\theta - \mathbf{i}_r N_r\}(a/r_a)^2, \quad r_a > a_0\end{aligned} \tag{23}$$

where

$$\mathbf{r}_a = \mathbf{i}_r r_a = \mathbf{j}(y_a - \eta) + \mathbf{k}(z_a - \zeta)$$

and

$$\mathbf{i}_\theta \cdot \mathbf{i}_r = 0$$

The term r_a is the radial distance from the doublet to the circle center.

If the body is slender and the doublets lie close to the body, the total force and moment can be assumed to act at the same longitudinal location x as that of the pressure doublet ξ. Distributions obtained in this way for other more general conditions tend to be too abrupt, even though the total force and moment are correct. If in flutter, gust, or frequency response analyses the important generalized forces are the total force and moment, this abruptness will not be important. However, the details of the distributions tend to be inaccurate.

The distribution can be obtained accurately only if the integration is done circumferentially. This produces a force per unit length distribution on the body. Equation (20) cannot be integrated exactly, even for a circular cross section; however, Lawrence and Flax[29] have presented an approximate expression for the steady case (only for the case of vertical force due to a z-oriented doublet). It has been found that if their approximate expression is integrated again in the longitudinal direction, from $+\infty$ to $-\infty$ with the circular radius a held constant, the total force is exactly correct for all values of r_a. Thus, an approximate force distribution integrates to give the exact force and moment.

This encouraging result led the authors to attempt the same approximate circumferential integration for the unsteady case. The basic approach is to: 1) expand $\exp[-i\lambda R]$ in terms of $\lambda r_a a_0 \beta^2 \cos\theta/R_a$, 2) for the case $r_a > a_0$, expand R in terms of $\beta^2 a_0 r_a/R_a^2$, 3) retain only lowest-order terms, and 4) integrate around circular cross section. Details of this integration are given in Ref. 22, Appendix G, and the result is

$$\frac{\partial(\mathbf{F}/q)}{\partial x} = \mathbf{N}\frac{\Delta C_p \delta A}{4}\beta^2 {a_0}^2\left\{\frac{1}{{R_a}^3} + \frac{i\lambda}{{R_a}^2}\right\} \times \exp\{i\lambda[M(x-\xi) - R_a]\} + \Delta \tag{24}$$

where $\Delta = 0$ for $r_a < a_0$, and*

$$\Delta = -N_r \dot{i}_r \frac{\Delta C_p \delta A}{4} \beta^2 {a_0}^2 \times \left[\left\{\frac{1}{{R_a}^3} + \frac{i\lambda}{{R_a}^2}\right\}\left\{\frac{i\lambda {r_a}^2 \beta^2}{R_a} + \frac{3\beta^2 {r_a}^2}{{R_a}^2}\right\} - \frac{i\lambda \beta^2 {r_a}^2}{{R_a}^4}\right] \times \exp\{i\lambda[M(x-\xi) - R_a]\}, \quad r_a > a_0 \quad (25)$$

where ${R_a}^2 = (x-\xi)^2 + \beta^2 {r_a}^2$. When Δ is zero ($N_r = 0$ or $r_a < a_0$), Eq. (24) can be integrated longitudinally to give the total lift. The result is

$$\mathbf{F}/q = \int_{-\infty}^{\infty} \partial(\mathbf{F}/q)/\partial x dx = \mathbf{N} \frac{\Delta C_p \delta A}{2} \left\{\frac{a_0}{r_a}\right\}^2 \left\{\frac{i\pi \bar{k}}{2} H_1^{(2)}(\bar{k})\right\} \quad (26)$$

when $\Delta = 0$.

For the case where $\Delta \neq 0$, it must be integrated numerically. The results obtained in Eq. (26) and the results of numerically integrated Δ can be compared with the exact results of Eq. (21) (numerically integrated around the circular cross section). As in the steady case, the approximate and exact results are the same. It must be remembered that although the total force is correct, the distribution is still only approximate.

In the present method the force distribution along the body axis is given, not as a continuous function, but at discrete points along the body axis. Specifically, the midpoints of the slender body elements are used for this purpose. To find the average force acting on a slender body element, Eqs. (24) and (25) must be integrated over the element. To perform this integration, it must be assumed that the slender body element is small compared with the wave length $2\pi/\omega$. The exponential term may then be expanded in series. The results are presented in Ref. 22, Appendix H.

In summary, two methods have been presented for determining the force distribution on a body. In one case the total force and moment due to a single pressure panel are lumped** at one point on a body of general cross section (method to be called Alternate II), while in the other case a distribution is found for the special case of a body of circular cross section (Alternate I). An approximate distribution can be generated for the first case where no distribution exists,†† by assuming the total force to be caused by an internal pressure doublet lying along the body axis, and by further assuming that Eq. (24) can then be applied using an average body radius, $a_0 = (a_0 + b_0)/2$. Even though the results of this approximation (to be called Alternate II redistributed) seem to agree well with experiment, it must be considered only as a temporary solution.

Calculated Results

Effect of Cross-Sectional Aspect Ratio (b/a)

Several studies were conducted to ascertain the effects of various body parameters on wing-body loadings; however, only one is presented to serve as an example. The effect of fuselage cross-sectional aspect ratio, b/a, on the wing loading is presented in Fig. 3.

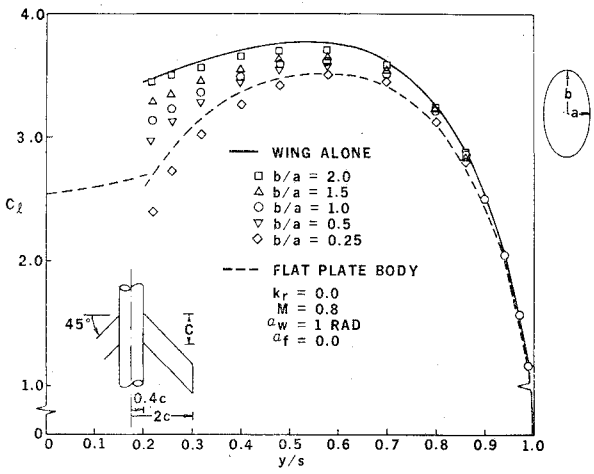

Fig. 3 Effect of fuselage cross-sectional aspect ratio (b/a) on the lift coefficient distribution of the wing.

The distribution of lift coefficient for a wing-fuselage combination is presented for the cross-sectional aspect ratio, b/a, in the range zero to infinity. The semiwidth a is constant and equal to $0.2s$ for all calculations. The case $b/a = 0.0$ is special and is obtained by replacing the body by a flat-lifting surface. The case $b/a = \infty$ is also special and is obtained by placing a plane of symmetry at the wing root (this case is given the designation of "wing alone"). All of the intermediate cases which are not special should lie within the envelope formed by the two special cases described above, however the curve corresponding to the lowest value of $b/a(=0.25)$ does not. The curve corresponding to the highest value of $b/a(=2.0)$ still lies inside the envelope but comes very close to passing outside of it. The upper bound of validity, for b/a of the present method, is then somewhere near or below 2.0. The lower bound of validity for b/a is somewhere between 0.5 and 0.25. If configurations that fall outside of this range are to be analyzed, it is recommended that either the body be replaced by a lifting surface ($b/a < 0.5$), or by a plane wall for ($b/a > 2.0$). An additional alternate is to place lifting surface singularities on the body surface in addition to, or in place of, the image system.

If the left-hand wing half is omitted from the calculation, then the effect of body end-plating can be ascertained. It is expected that the end-plating effects, as obtained by the Present Method, will be slightly smaller than they should be when $b/a > 1$. Two reasons are offered for this: 1) the image within the ellipse is cut off once it crosses the $y = 0$ plane, and 2) the interference singularities cannot account for an onset flow whose average, $\overline{\delta w}$, is zero (i.e., a flow that is antisymmetric across the body). If the body were circular, then the image would fully account for the end-plating effect and the axial singularities would properly account for interference. Also, if $b/a < 1$ the effect of the body is properly accounted for. However, for the $b/a > 1$ case, some of the end-plating effect may be lost due to the approximated and abbreviated image system. If one further term is added to the multipole series of the residual flow, then this loss of end-plating could be recaptured, even for highly elliptic cases. In addition, the resistance of the fuselage to roll could be calculated.

Wing-Fuselage Combinations

Four different methods for calculating the steady flow about wing-fuselage combinations are compared in Fig. 4. The original version of this figure appeared in Ref. 11 without the results of the Present Method. The configuration consists of a simple swept wing attached to a very large-diameter

* The local radius a_0 is used when pressures are calculated and not the average tube radius, a. The radial distance r_a of image doublets, calculated using the average radius a, are legislated to lie inside the slender body, i.e., $r_a < a_0$.

** The force is actually spread out over the slender body element over which it acts.

†† A distribution will be generated for this case because there is a distribution of pressure doublets, however, there is no distribution for one pressure doublet.

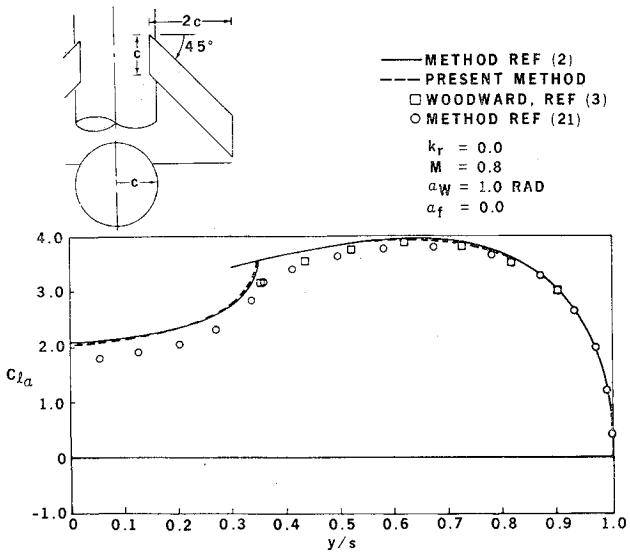

Fig. 4 Comparison of the lift-curve-slope distribution as calculated by the present method and various other methods for a wing-fuselage combination.

circular fuselage. The wind is at one radian angle-of-attack, while the fuselage is held to zero incidence. All methods are in good agreement. However, the present method is in better agreement with the method of Ref. 2, while the Woodward method is in better agreement with the method of Ref. 21. The method of Ref. 21, like Woodward's method, uses lifting surface elements on the body surface and predicts a lift coefficient distribution that lies slightly below that of the present method. This is expected since lifting surface elements placed on the body surface are less effective in accounting for interference than are images.

A wing-fuselage comparison presented in Ref. 2 is represented in Fig. 5. In addition, a calculation using the Present Method is shown. The span load for a wing (at 4.7° angle-of-attack) attached to a circular fuselage (at 0.7° angle-of-attack) is given in this figure. The agreement between the Present Method and the method of Ref. 2 is excellent, as is the correlation with the experimental data.[30] Since this is a steady case, the agreement between the two methods should be perfect; however, a change in the number of spanwise strips near the tip has caused a slight disparity.

Figure 6 presents a correlation of the Present Method with the experimental data of Körner[31] and the theory of Labrujere[15] et al. The configuration considered is a straight wing-fuselage combination ($D/C = 1.0$) at an angle-of-attack of 6°. The experimental data in Fig. 6 lie below the calculated results, giving a clear indication of viscous effects. The distribution calculated by the Present Method lies almost equidistant between the data and the calculated results of Labrujere. The discontinuity in span load apparent in the theory of Labrujere is caused by the fact that the fuselage does not close due to the wind tunnel sting; thus, there exists a resultant slender body lift. The reason the Present Method and the method of Labrujere are in slight disagreement is because wing thickness effects are accounted for by the latter method, thus rendering the wing more effective in lift.

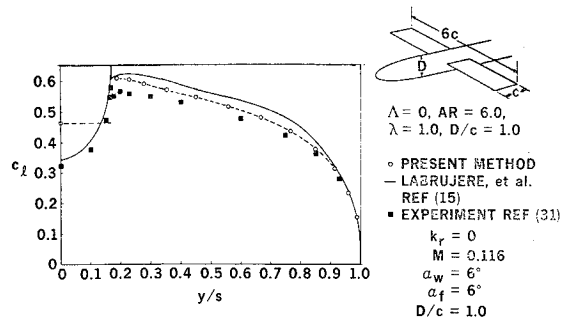

Fig. 6 Comparison of experimental and calculated lift coefficient distributions for a straight-wing/fuselage combination.

Results for a swept wing-fuselage combination are presented in Fig. 7. The wing and fuselage are at 6° and 0° incidence, respectively. The longitudinal distribution of force on the fuselage, as calculated and as obtained experimentally, are shown in the figure. Two calculations are shown and both are in good agreement with the experimental data.

Figure 8 presents a comparison of experimental and calculated fuselage force distribution for a typical transport aircraft flying at $M = 0.6$. The two calculation methods shown are in good agreement with the experiment. The lack of pressure recovery in the empennage area accounts for the difference between the data and the calculated results.

Figure 9 presents a comparison of the loading on a T-tail as calculated by the Present Method, the method of Zwaan,[8] and experimental data. Results for two configurations are shown: one for the T-tail and fuselage, and one for the T-tail and a ground plane. The experimental data were taken for the fuselage case and are in good agreement with the present method and the method of Zwaan except near the fuselage intersection. The case with the ground plane is presented to illustrate the effect of the fuselage. Zwaan used a small extension of the vertical fin to represent the fuselage.

Wing and Tip-Mounted Nacelle Combination

The only experimental data that have been found for a wing/body configuration in oscillatory motion are reported

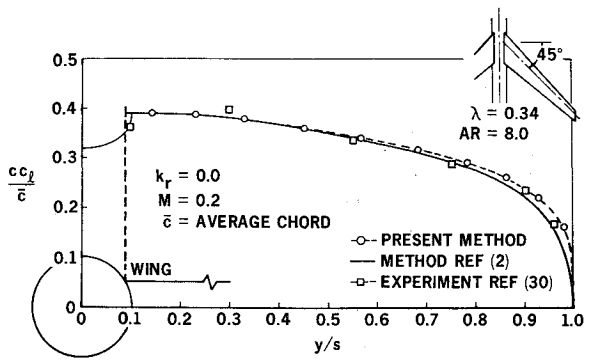

Fig. 5 Comparison of experimental and calculated span load for a wing-fuselage combination.

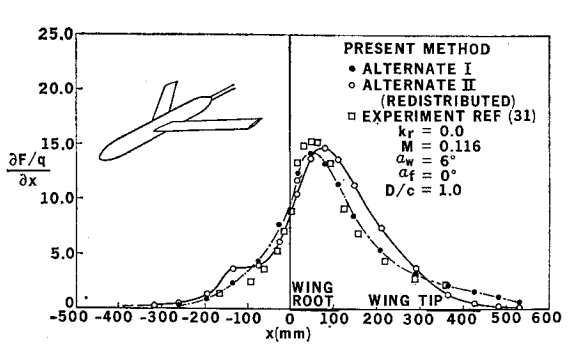

Fig. 7 Comparison of experimental and calculated fuselage load distribution (fuselage at zero incidence).

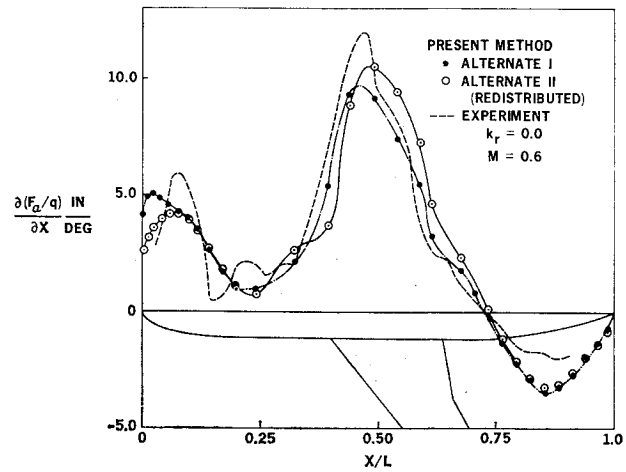

Fig. 8 Comparison of experimental and calculated fuselage load distribution for a Mach number of 0.6.

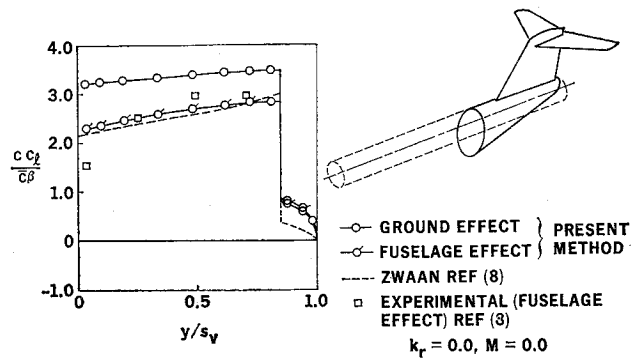

Fig. 9 Comparison of experimental and calculated span load for a *T*-Tail/Fuselage combination in steady flow.

by Cazemier and Bergh.[32,33,34] A wooden model of a low-aspect-ratio wing, fitted with a large wing-tip nacelle ($b/a = 2$) was tested over a wide range of frequencies. The wind tunnel Reynolds number was low ($Re = 4.7 \times 10^6$/m) and the model was approximately 1 m in semispan. The test was set up to read the lifting pressure directly. The pressures were transmitted from the model through tubes calibrated to eliminate the phase shift caused by the transmission time required to communicate the pressure from the model to the pickup point.

The first comparison presented for this configuration is given in Fig. 10. The lift coefficient distribution is shown for the steady case. The upper plot gives a comparison of lift coefficient, as calculated by the present method, and as determined experimentally for the wing-alone case. The agreement is generally good except for the strange fact that the experimental data lie above the calculated results. The lower plot presents a similar comparison for the wing/nacelle case‡‡ and contains two curves marked "Present Method."

The results of the unmodified Present Method are presented in the lower of the two curves. The upper curve is obtained when lifting surface elements are placed on the body surface, in conjunction with images, in the Present Method, and is in better agreement with the data. The results of the upper curve are obtained at the cost of doubling the number of unknowns in the problem. Thus, accuracy and efficiency must be balanced by the user of the present method. Also shown on the wing/nacelle (lower) plot is the wing-alone case. There is a very large difference between the wing-alone and wing/nacelle lift coefficient distributions. The unmodified Present Method predicts most of the nacelle effect, even when lifting surface elements are not placed on the body surface.

Figure 11 presents a comparison of experimental and calculated lifting pressure for two modes of motion for the wing without the nacelle. The agreement is better for the flap case (the flap is the inboard control surface) than for the case of roll.

Figure 12 presents a comparison of experimental data and calculated results for the wing-nacelle combination oscillating in several rigid body modes (pitch, plunge, roll). The reduced

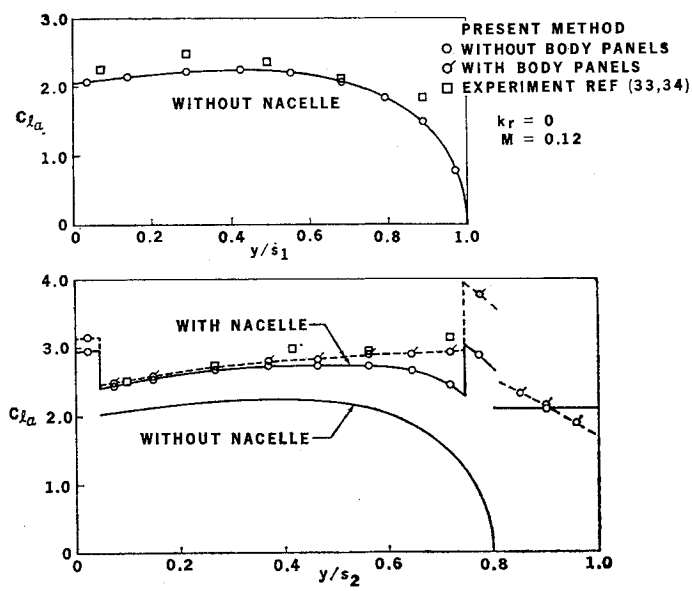

Fig. 10 Comparison of experimental and calculated lift-curve-slope distributions for the V.J. 101-C with and without Nacelle in steady flow.

‡‡ The wing is slightly different in the wing-alone and wing-nacelle cases (see Figs. 11 and 12). The reason for the discontinuities in c_{l_α} in Fig. 10 (lower plot) is the discontinuity in chord length in those regions.

frequency, based on a normal semispan of 1.097m, i.e., $k_r = \omega 1.097/2U$ is 1.0. The agreement between experimental and theoretical results is approximately the same as that obtained for the nacelle-off case.

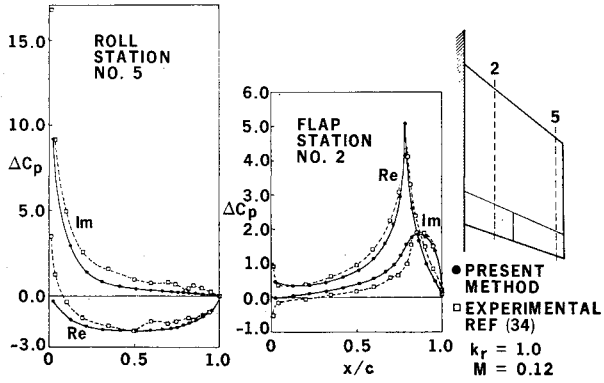

Fig. 11 Comparison of experimental and calculated lifting pressure distributions for the V.J. 101-C wing alone. (Roll and oscillating flap, $k_r = 1.0$).

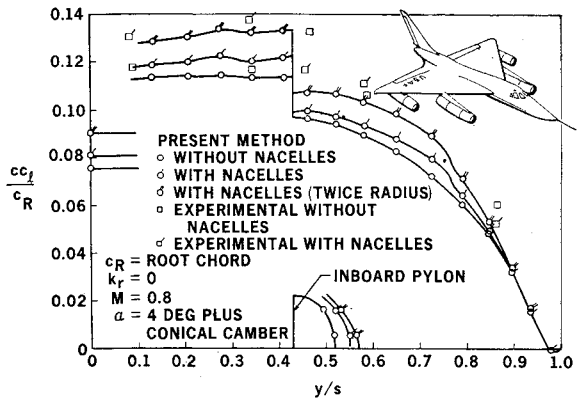

Fig. 13 Comparison of experimental and calculated span loading on the B-58 aircraft for various nacelle diameters.

Wing-Nacelle-Fuselage Combination

A good example of a complex wing-nacelle-fuselage combination is found in the B-58 bomber. A detailed description of the configuration is found in Ref. 35. A comparison of the present method with experimental data for the configuration with and without nacelles is presented in Fig. 13. Specifically, the span load for the wing at 4° angle-of-attack (in addition to conical camber) is presented. The experimental data lie above the calculated values. Similar results were obtained by Bradley and Miller.[36] The cause of this is found in the very high sweep of the leading edge. As is well known, wings with large leading edge sweep angles develop a leading edge vortex which causes an increase in the lift.

The effect of nacelle size is also given in this figure. Shown are the span loads on the wing and inboard pylon (the outboard pylon is omitted since it is small) for three different nacelle sizes: normal diameter, twice diameter and nacelles off (diam = 0). This figure shows that the nacelles have a significant interference effect on the wing loading.

Concluding Remarks

A method for predicting oscillatory loads on very general configurations has been developed. Configurations may include a combination of any or all of the following components: 1) lifting surfaces such as wings, pylons, stabilizer, and fin with arbitrary dihedral, partial or full span control surfaces, and 2) bodies such as fuselages, nacelles, stores with elliptic cross-section shapes. The operating conditions are also very general: 1) all frequencies of practical interest and all subsonic Mach numbers, 2) symmetry and ground effect, 3) mutual interference of lifting surfaces, and 4) multiple modes of oscillation.

Because an image approach is used, the body cross-sectional aspect ratio b/a cannot take extreme values. Specifically, it must lie in the range of 0.5 to 2.0.

If conditions or configurations are simple, then other methods may be used to compare with the present method. Cases which involve only lifting surfaces may be handled by the methods of Laschka[7] and Zwaan.[8] Comparisons of these methods (Ref. 23 presents comparisons with Laschka's method) with the Present Method show good agreement. For the steady case, the theories of Woodward[3] and Labrujere[15] may also be used for comparison. Loads predicted by the present method fall slightly below those predicted by the steady incompressible theory of Labrujere because of wing thickness effects which are not accounted for by the Present Method. Loads predicted by the Present Method lie above those predicted by Woodward and the method of Ref. 21 because lifting surface elements placed on the body surface are not usually as effective as images in accounting for interference. The results are highly dependent on the idealization. If the cross section is represented by only a few elements, the results can be inaccurate, especially for unsteady flow.

Several methods have been proposed for the determination of body loads. The total force and moments are predicted accurately in all cases. Also, the longitudinal distribution of load is predicted accurately for bodies of circular cross section. However, for bodies of noncircular cross section the distribution of load is not predicted as accurately as desired. Although the technique of redistributing these loads seems to give good results for the cases presented, improvement of this method is a subject for further investigation.

Generally, the agreement of the present method with experimental data is good. In cases where the Reynolds number is low, the classic viscous loss of lift is observed.

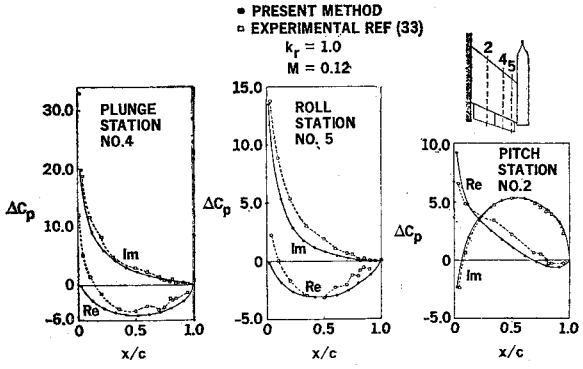

Fig. 12 Comparison of experimental and calculated lifting pressure distributions for the V.J. 101-C wing-nacelle combination (pitch, plunge, roll, $k_r = 1.0$).

References

[1] Hedman, S. G., "Vortex Lattice Method for Calculation of Quasi Steady State Loadings on Elastic Wings in Subsonic Flow," Rept. FAA 105, Oct. 1965, Aeronautical Research Inst. of Sweden, Stockholm.

[2] Giesing, J. P., "Lifting Surface Theory for Wing-Fuselage Combinations," Report DAC-67212, Aug. 1968, McDonnell Douglas Corp., Long Beach, Calif.

[3] Woodward, F. A., "Analysis and Design of Wing-Body Combinations at Subsonic and Supersonic Speeds," *Journal of Aircraft*, Vol. 5, No. 6, Nov.–Dec. 1968, pp. 528–534.

[4] Spangler, S. B. and Mendenhall, M. R., "Theoretical Investigation of Ducted Fan Interference for Transport-Type Aircraft," *NASA Symposium on Analytic Methods in Aircraft Aerodynamics, 28–30 October, 1969*, Paper 30, NASA SP-228, pp. 703–719.

[5] Borland, C. J., "Methods of Calculating Aerodynamic Loads

on Aircraft Structures: Part I—Wing-Body Interference Effects," AFFDL-TR-66-37, Pt. I, Aug. 1966, Air Force Flight Dynamics Lab., Wright-Patterson Air Force Base, Ohio.

[6] Chou, D. C., "Methods of Calculating Aerodynamic Loads on Aircraft Structures: Part III—Effects of Engines, Stores and Wing-Tail Interference," AFFDL-TR-66-37, Pt. 3, May 1966, Air Force Flight Dynamics Lab., Wright-Patterson Air Force Base, Ohio.

[7] Laschka, B., "Interfering Lifting Surfaces in Subsonic Flow," AGARD Structures and Material Panel Meeting, Istanbul, Turkey, Sept.–Oct. 1969, Vereinigte Flugtechnische Werke, Munich, Germany.

[8] Zwaan, R. J., "Calculated Results for Oscillating T-Tails in Subsonic Flow and Comparison with Experiments," NLR Rept. MP 253, Aug. 1967, National Aerospace Lab., Amsterdam, The Netherlands.

[9] Albano, E. and Rodden, W. P., "A Doublet-Lattice Method for Calculating Lift Distributions on Oscillating Surfaces in Subsonic Flows," *AIAA Journal*, Vol. 7, No. 2, Feb. 1969, pp. 279–285; also Errata, *AIAA Journal*, Vol. 7, No. 11, Nov. 1969, p. 2192.

[10] Stark, V. J. E., "Aerodynamic Forces on a Combination of a Wing and Fin Oscillating in Subsonic Flow," Rept. TN-54, 1964, Saab Aircraft Co., Linköping, Sweden.

[11] Kálmán, T. P., Rodden, W. P., and Giesing, J. P., "Application of the Doublet-Lattice Method to Nonplanar Configurations in Subsonic Flow," *Journal of Aircraft*, Vol. 8, No. 6, June 1971, pp. 406–413.

[12] Albano, E., Perkinson, F., and Rodden, W. P., "Subsonic Lifting-Surface Theory Aerodynamics and Flutter Analysis of Interfering Wing/Horizontal-Tail Configurations," Part I, Subsonic Oscillatory Aerodynamics for Wing/Horizontal-Tail Configurations, AFFDL-TR-70-59, Pt. I, Sept. 1970, Air Force Flight Dynamics Lab., Wright-Patterson Air Force Base, Ohio.

[13] Rodden, W. P., Giesing, J. P., and Kálmán, T. P., "New Developments and Applications of the Subsonic Doublet-Lattice Method for Nonplanar Configurations," AGARD-CP-80-71, Paper 4, *AGARD Symposium on Unsteady Aerodynamics for Aeroelastic Analyses of Interfering Surfaces*, Tonsberg, Oslofjorden, Norway, Nov. 3–4, 1970.

[14] Rubbert, P. E. and Saaris, G. R., "A General Three-Dimensional Potential Flow Method Applied to V/STOL Aerodynamics," S.A.E. Paper 680304, 1968, Boeing Aircraft Co., Seattle, Wash.

[15] Labrujere, T. E., Loeve, W., and Slooff, J. W., "An Approximate Method for the Calculation of the Pressure Distribution on Wing-Body Combinations at Subcritical Speeds," AGARD Specialist Meeting on Aerodynamic Interference, Silver Spring, Md., 28–30 Sept. 1970, *AGARD Conference Proceedings No. 71*; also NLR MP 70014U, 1970, National Aerospace Lab., Amsterdam, The Netherlands.

[16] Hess, J. L., "Calculation of Potential Flow About Arbitrary Three-Dimensional Lifting Bodies," Phase II Final Report, Douglas Rept. MDC-J0971-01, Oct. 1970, Douglas Aircraft Co., Long Beach, Calif.

[17] Giesing, J. P., "Two-Dimensional Potential Flow Theory for Multiple Bodies in Small-Amplitude Motion," *AIAA Journal*, Vol. 8, No. 11, Nov. 1970, pp. 1944–1553.

[18] Monical, R. E., "A Method for Representing Fan-Wing Combinations for Three-Dimensional Potential Flow Solutions," *Journal of Aircraft*, Vol. 2, No. 6, Nov.–Dec. 1965, pp. 527–530.

[19] Tulinius, J. R., "Theoretical Prediction of Thick Wing and Pylon-Fanpod-Nacelle Aerodynamic Characteristics at Subcritical Speeds," Rept. NA-71-447, June 1971, North American Rockwell, Los Angeles, Calif.

[20] Rodden, W. P., Giesing, J. P., and Kálmán, T. P., "Refinement of the Non-planar Aspects of the Subsonic Doublet-Lattice Lifting Surface Method," *Journal of Aircraft*, Vol. 9, No. 1, Jan. 1972, pp. 69–73.

[21] Giesing, J. P., Kálmán, T. P., and Rodden, W. P., "Subsonic Unsteady Aerodynamics for General Configurations," Part I, Direct Application of the Nonplanar Doublet Lattice Method, AFFDL-TR-71-5, Pt. I, Feb. 1971, Air Force Flight Dynamics Lab., Wright-Patterson Air Force Base, Ohio.

[22] Giesing, J. P., Kálmán, T. P., and Rodden, W. P., "Subsonic Unsteady Aerodynamics for General Configurations," Part II, Application of the Doublet-Lattice Method and the Method of Images to Lifting-Surface/Body Interference," AFFDL-TR-71-5, Part II, Dec. 1971, Air Force Flight Dynamics Lab., Wright-Patterson Air Force Base, Ohio.

[23] Kálmán, T. P., Rodden, W. P., and Giesing, J. P., "Aerodynamic Influence Coefficients by the Doublet Lattice Method for Interfering Nonplanar Lifting Surfaces Oscillating in a Subsonic Flow," Douglas Rept. DAC-67977, Nov. 1969, Douglas Aircraft Co., Long Beach, Calif.

[24] Miles, J. W., "On Non-Steady Motion of Slender Bodies," *Aeronautical Quarterly*, Vol. II, Nov. 1950, pp. 183–194.

[25] Lennertz, J., "On the Mutual Reaction of Wings and Body," TM 400, 1927, NACA.

[26] Durand, W. F., "Influence of the Propeller on Other Parts of the Airplane Structure," *Aerodynamic Theory*, edited by F. W. Durand, Vol. 4, Springer, Berlin, 1935.

[27] Rethorst, S., "Aerodynamics of Nonuniform Flows as Related to an Airfoil Extending Through a Circular Jet," *Journal of Aeronautical Sciences*, Vol. 25, No. 1, Jan. 1958, pp. 11–28.

[28] Wu, T., Y.-T. and Talmadge, R. B., "A Lifting Surface Theory for Wings Extending Through Multiple Jets," Vehicle Research Corporation, Rept. No. 8, Aug. 1961, Vehicle Research Corp., Pasadena, Calif.

[29] Lawrence, H. R. and Flax, A. A., "Wing-Body Interference at Subsonic and Supersonic Speeds—Survey and New Developments," *Journal of the Aeronautical Sciences*, Vol. 21, Nov. 5, May 1954.

[30] Martina, A. P., "The Interference Effect of a Body on the Spanwise Load Distribution of Two 45-Degree Sweptback Wings of Aspect Ratio 8.02 from Low-Speed Tests," TN 3730, Aug. 1956, NACA.

[31] Körner, H., "Untersuchungen zur Bestimmung der Druckverteilung an Flügel-Rumpf-Kombinationen. Teil I: Messergebnisse fur Mitteldeckeranordung aus dem 1.3m—Wind-kanel," DFVLR—Report No. 0562, June, 1969, Deutsche Forschungs-Und Versuchsanstalt Für Luft-und Raumfahrt, E.V., Braunschweig, Germany.

[32] Cazemier, P. G. and Bergh, H., "Messungen Instationärer Druckverteilungen am Flügelhalbmodell der V.J. 101-C," NLR Rept. F.232, Oct. 1964, National Aerospace Lab., Amsterdam, The Netherlands.

[33] Bergh, H. and Cazemier, P. G., "Ergebnisse der Instationären Druckmessungen am Flügelhalbmodell der V.J. 101-C mit Triebwerksgondel," NLR, F.233, May 1963, National Aerospace Lab., Amsterdam, The Netherlands.

[34] Bergh, H. and Cazemier, P. G., "Ergebnisse der Instationären Druckmessungen am Flügelhalbmodell der V.J. 101-C ohne Triebwerksgondel," NLR F.234, May 1963, National Aerospace Lab., Amsterdam, The Netherland.

[35] Walker, C., "Summary Report of Wing Tunnel Tests on a 1/17-Scale Pressure Model of the Project MX-1964 Airplane at the 10-Foot Transonic Tunnel of WADC," Convair-Fort Worth, Rept. FZT-4-102, Sept. 1955, Fort Worth, Texas.

[36] Bradley, R. G. and Miller, B. D., "Application of Finite-Element Theory to Airplane Configurations," *Journal of Aircraft*, Vol. 8, No. 6, June 1971, pp. 400–405.